

# Multi-channel Optical Vision Model

Ali Momeni<sup>1</sup>, Guillaume Noetinger<sup>1</sup>, Tim Tuuva<sup>1</sup>, and Romain Fleury<sup>1,\*</sup>

<sup>1</sup>*Laboratory of Wave Engineering, School of Electrical Engineering, Swiss Federal Institute of Technology in Lausanne (EPFL), Lausanne, Switzerland*

*\*E-mail: romain.fleury@epfl.ch*

## Abstract

Spatial multiplexing is one of the natural strengths of optics, yet in optical neural networks it is often used mainly as parallel throughput. Here we show that spatial multiplexing in an optical neural network can be used not only to process multiple inputs in parallel, but also to define a trainable representational coordinate of the model. In three implemented scenarios, parallel-input processing, class-code readout and channel-mixed feature interaction, spatial channels act as independent learners, structured code dimensions and interacting feature groups. The programmable free-space optical processor is trained through an online physical-forward/surrogate-backward scheme, where measured optical outputs define the forward pass while a differentiable surrogate estimates gradients and is continually fine-tuned during training from newly acquired optical data. We demonstrate these channel roles in image-classification and regression tasks using multi-layer architectures with more than one million trainable optical phase parameters. We further implement a hybrid optical-electronic vision-language model, in which the optical neural network provides visual tokens to a digital transformer decoder for controlled image-captioning tasks. These results establish spatially multiplexed optical channels as a programmable feature and readout space for hybrid optical vision models.

# Introduction

Modern vision models, including convolutional neural networks and more recent vision transformers, rely on dense numerical operations, repeated memory access and increasingly large training and inference pipelines<sup>1-3</sup>. This computational load places growing pressure on conventional electronic hardware, particularly when visual or multimodal inputs must be encoded, moved through memory and transformed repeatedly before a final decision is made<sup>4-6</sup>. Optical and photonic systems offer a complementary computational substrate in which diffraction, interference, modulation and detection act directly on high-dimensional spatial fields. This makes optics naturally suited to visual processing: an image is already a spatial field, and optical propagation can transform many spatial degrees of freedom in parallel. The central question is therefore not only whether optics can accelerate isolated linear operations, but whether programmable optical systems can be trained as visual front ends whose physical degrees of freedom participate in representation learning.

Optical neural networks have advanced along several directions. Diffractive and free-space optical processors have shown that cascaded optical layers can implement learned spatial transformations and task-specific inference<sup>7-10</sup>. Integrated photonic systems have demonstrated optical acceleration of matrix multiplication, convolution, and neural-network primitives, with high bandwidth and compact implementations<sup>11-15</sup>. Optical and optoelectronic vision processors further suggest that computation can be embedded into sensing or analog front ends<sup>16,17</sup>. At the training level, physical neural networks and forward-mode optical training have emphasized that measured hardware responses can be included directly in optimization, reducing the mismatch between idealized simulation and experimental behavior<sup>18,19</sup>. Related work has also examined backpropagation-free physical learning, broader training strategies for physical neural networks, programmable-metasurface expressivity, and nonlinear time-Floquet wave learning<sup>20-23</sup>. Recent work on nonlinear encoding, optical transformers, large-scale photonic accelerators, and optical generative models points toward more complex optical AI workflows<sup>24-29</sup>. However, spatial multiplexing in many demonstrations remains closer to parallel throughput, independent sensing, or task-specific readout than to a trainable representational axis.

The key challenge is therefore not only to build larger optical processors, but to define optical architectures in which multiplexed channels carry structured computational meaning. This reveals a fundamental challenge: multi-channel optical representation learning must be realized directly on imperfect physical hardware, where experimental constraints and system nonidealities play a central role, rather than in idealized simulations alone. Training such systems requires end-to-end optimization through the physical hardware while accounting for channel-dependent aberrations, finite modulator and detector precision, optical cross-talk, measurement noise, fluctuations in signal-to-noise ratio, and laser drift. It also requires a differentiable interface that scales across channels. Training an independent surrogate for each channel would discard the shared structure of optical propagation and would scale poorly with channel number. A single channel-conditioned surrogate offers a practical way to share information across channels while retaining channel-specific corrections, and online fine-tuning can update this surrogate from measured input-output pairs collected during training.

Here we show that spatial multiplexing in an optical neural network can be used not only to process multiple inputs in parallel, but also to define a trainable representational coordinate of the model. We experimentally implement a multi-layer and multi-channel optical vision architecture trained through an online physical-forward/surrogate-backward scheme, in which measured optical outputs define the forward pass and a differentiable surrogate supplies gradients while being continually updated from optical data. The optical layers also use an input-dependent structural nonlinearity at the spatial light modulators (SLM) plane, where the channel input is embedded into the displayed physical phase modulation. We investigate three scenarios of channel-based computation: parallel-input processing, where spatial channels act as independent optical learners; class-code readout, where channels form structured code dimensions for classification; and channel-mixed feature interaction, where measured channel outputs are coupled between optical layers. We demonstrate these roles on benchmark vision tasks including handwritten-digit classification (MNIST), fashion-item classification (Fashion-MNIST), and facial keypoint regression, using multi-layer optical architectures with more than one million trainable phase parameters. We further extend

the framework to a hybrid optical-electronic vision-language model, in which the optical neural network provides visual tokens to a digital transformer decoder for controlled image captioning. Together, these results establish spatially multiplexed optical channels as a programmable feature and readout space for hybrid optical vision models.

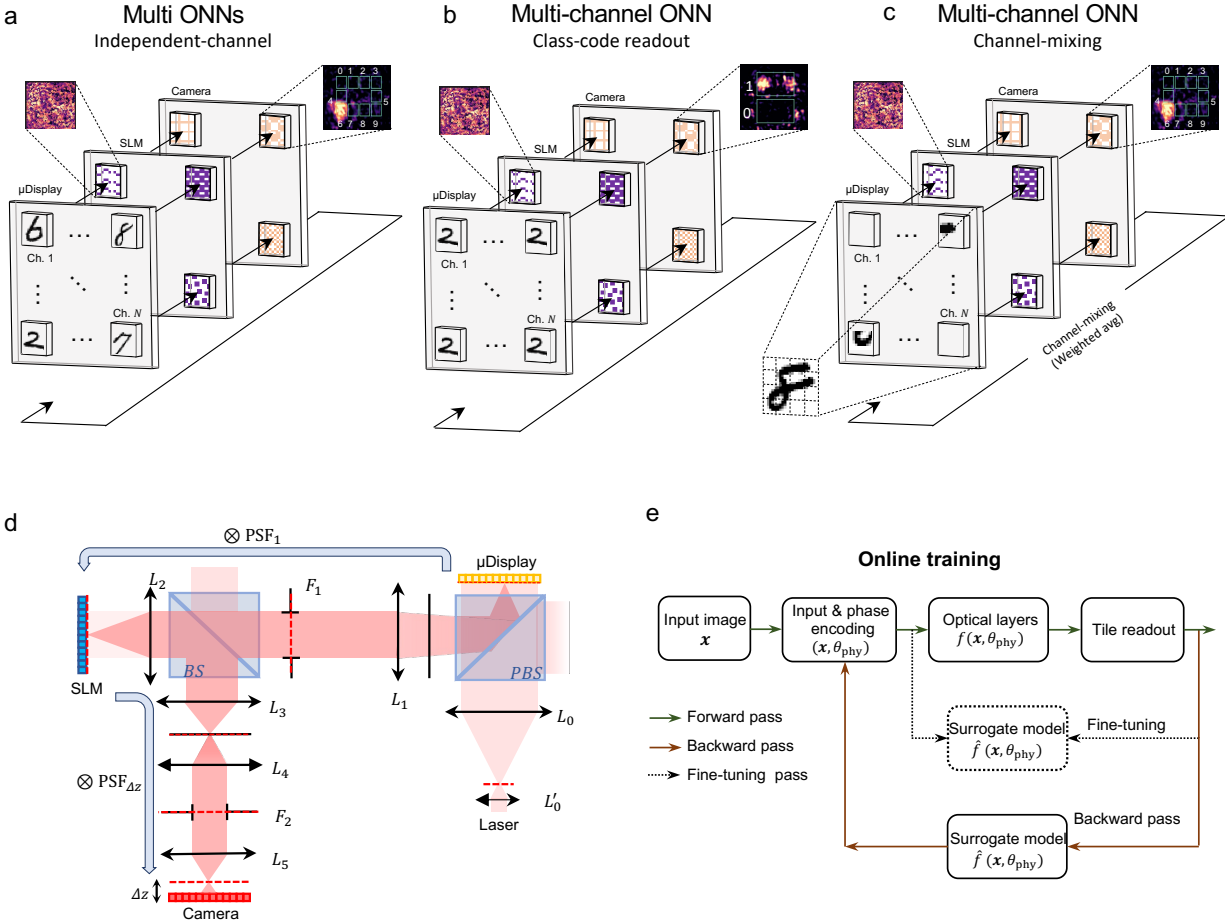


**Figure 1. Multi-channel optical vision model and experimental training workflow.** **a**, Independent-channel multi-ONN readout. Different input samples are assigned to spatial channels on the microdisplay, encoded by channel-specific phase masks on the SLM, propagated through the free-space optical stack, and measured as separate camera-output tiles. Each channel can therefore act as an independent optical learner. **b**, Class-code readout. The same input image is repeated across optical channels, and the measured channel outputs are converted into bit-like readout margins that are decoded against a class code. **c**, Channel-mixing mode. A single input image is partitioned into spatial patches that populate multiple channels, and measured channel outputs are electronically mixed before being sent to the next optical layer. This electronic coupling lets distributed channel features interact while the optical transformations remain spatially multiplexed. **d**, Free-space optical implementation: an expanded laser beam is directed onto a liquid crystal amplitude modulator (*the microdisplay*) displaying the input data. The resulting field is sent to a phase-only SLM to apply some learnable weights in a conjugate plane. The modulated beam is then filtered and collected by a defocused camera. This entire optical path defines the measured optical forward pass. It is equivalent to the propagation in a slab with tunable transmission. **e**, Online physical-forward/surrogate-backward training. The optical system produces measured outputs during the forward pass, a single differentiable surrogate supplies gradients for backpropagation, and buffered optical input-output pairs are used to fine-tune the surrogate during training.

# Results

## Architecture and experimental setup

We first establish the architecture and training workflow of the proposed multi-layer, multi-channel optical vision model (Fig. 1). The system is formulated for  $N$  spatially multiplexed optical channels arranged as tiled fields on the input and output planes. In a general form, the field in channel  $c$ , with  $c = 1, \dots, N$ , at optical layer  $l + 1$  can be written as

$$\mathbf{x}_c^{(l+1)} = f\left(\mathbf{x}_c^{(l)}, \boldsymbol{\theta}_{\text{phys},c}^{(l)}\right), \quad (1)$$

where  $\mathbf{x}_c^{(l)}$  denotes the spatial intensity pattern encoded in channel  $c$  at layer  $l$ ,  $\boldsymbol{\theta}_{\text{phys},c}^{(l)}$  denotes the displayed trainable physical phase profile for that channel and layer, and  $f$  denotes the measured physical transformation including intensity encoding, phase modulation, free-space propagation, optical detection and camera readout. The demonstrations illustrated in Fig. 1a–c differ in how the channel inputs are defined and how the channel outputs are combined. In the parallel-input (independent-channel) scenario, different images are assigned to different channels,  $\mathbf{x}_c^{(0)} = \mathbf{I}_c$ , and each channel acts as an independent optical learner (Fig. 1a). The optical outputs are also read out independently, allowing each channel to produce its own prediction without requiring information from the other channels. In the MNIST demonstration shown in Fig. 1a, the camera readout associated with each channel is divided into ten spatial detector tiles, with each tile corresponding to one digit class. The integrated intensity measured within these tiles forms the channel-specific output vector, and the predicted class is obtained from the tile receiving the highest optical energy. Because the channels operate in parallel while sharing the same optical hardware, multiple images can be processed simultaneously, each with its own dedicated optical path, trainable phase masks and decision readout. In the class-code scenario, the same image is replicated across all channels,  $\mathbf{x}_c^{(0)} = \mathbf{I}$ , and each channel is read out through two spatial tiles that define a binary response; across channels, these responses form a structured multi-bit class code (Fig. 1b). In the channel-mixed

scenario, a single image is partitioned into channel-specific patches,  $\mathbf{x}_c^{(0)} = \mathcal{P}_c(\mathbf{I})$ , and the measured outputs are electronically mixed between layers as a weighted sum across channels (Fig. 1c). This last case is central to the representational use of multiplexing: information is not only read out from parallel channels, but exchanged across channels during the layered computation.

The experimental platform is a programmable free-space optical processor (Fig. 1d) made by the conjugation of an amplitude and a phase spatial light modulators (respectively named the *microdisplay* and *SLM* hereafter) sent to a defocused camera mimicking propagation through a diffractive layer with a tunable transmission (see Methods). Hence, successive propagations through the setup are equivalent to the propagation in a layered complex media with non-linearities, here the camera readout. In the experiments reported here,  $N = 16$  channels are arranged as a  $4 \times 4$  tiled optical field, they are aligned thanks to a semi-automatic procedure in order to have the same spatial response<sup>?</sup>. A laser-illuminated microdisplay encodes the channel intensity patterns, relay optics map the modulated light to the spatial light modulator, and channel-dependent trainable phase masks are applied before propagation to the camera. For a single channel  $c$  and optical layer  $l$ , the measured update can be written as an effective intensity-to-intensity transformation,

$$\mathbf{x}_c^{(l+1)} = \mathcal{D} \left[ \left| h_{\Delta z} * \left( \exp\left(i 2\pi \boldsymbol{\theta}_{\text{phys},c}^{(l)}\right) \odot \left[ h_1 * \mathcal{A}\left(\mathbf{x}_c^{(l)}\right) \right] \right) \right|^2 \right], \quad (2)$$

where  $\mathcal{A}$  denotes the display and illumination encoding,  $h_1$  and  $h_{\Delta z}$  are effective point-spread functions for the relay and propagation sections shown in Fig. 1d,  $\odot$  denotes pixelwise phase modulation on the spatial light modulator,  $*$  is the 2D convolution operator, and  $\mathcal{D}$  includes camera readout, cropping, normalization and preparation of the measured image for the next layer. This expression summarizes the optical computation performed by modulation, free-space propagation and intensity detection; during training, however, the forward value is the measured camera response of the physical system.

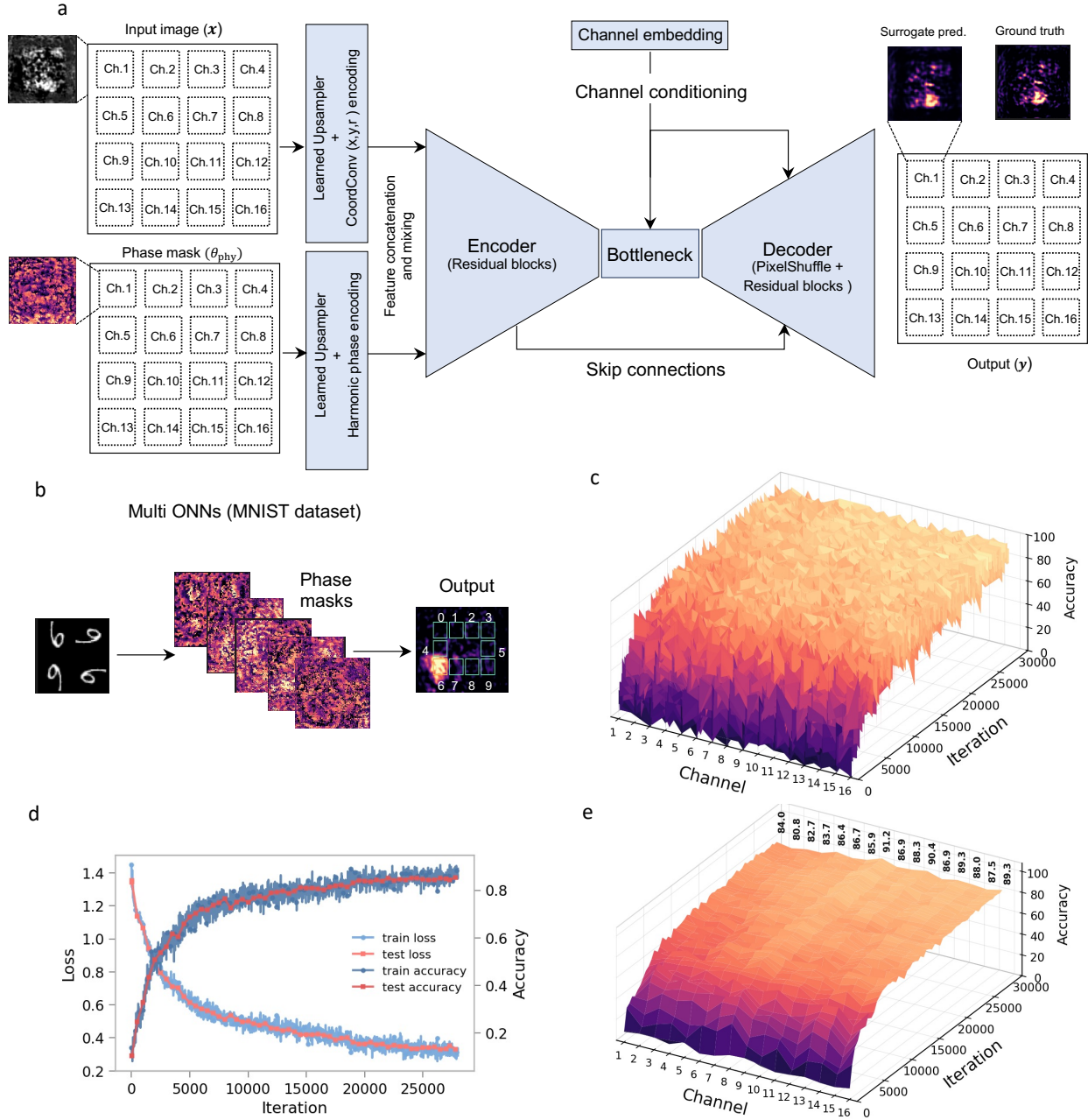


**Figure 2. Channel-conditioned surrogate model and MNIST multi-ONN training.** **a**, Surrogate architecture used to approximate the optical response across all 16 channels. The model encodes the input field and phase mask using learned upsampling, coordinate features, and multi-harmonic phase features, then predicts the camera-plane output with an encoder-decoder network, skip connections, and channel conditioning. Example surrogate predictions are compared with measured or reference optical outputs. **b**, Example five-layer MNIST multi-ONN inference, showing the tiled digit input, trainable phase masks, and camera-plane class readout. **c**, Channel-wise accuracy surface over training iteration for the 16 optical channels. **d**, Training and evaluation loss/accuracy curves computed from the weighted sum of different channel readouts, showing that all channels are trained together in one multi-channel ONN. **e**, Channel-wise performance map summarizing how the distribution of channel accuracies stabilizes during optimization.

Training is performed with an online physical-forward/surrogate-backward scheme (Fig. 1e). In the forward pass, the encoded input and displayed optical phase profile are sent through the physical processor, so that the layer output is the measured camera response,  $\mathbf{y}_{\text{phys}} = f(\mathbf{x}, \boldsymbol{\theta}_{\text{phys}})$ , rather than the output of a numerical optical model. For ONN training, a physics-informed differentiable surrogate  $\hat{f}(\mathbf{x}, \boldsymbol{\theta}_{\text{phys}})$  (Fig. 2a) is evaluated on the same encoded input and phase profile and is used only to supply gradients during the backward pass. Thus, the loss is computed from the measured optical readout, while the parameter update is obtained through the surrogate approximation. This workflow enables multi-layer optical architectures with more than one million trainable phase parameters to be optimized directly through measured optical forward passes.

The surrogate uses the intensity-to-intensity model in Eq. 2 as an approximate optical model: measured point-spread-function (PSF) kernels corresponding to the relay and propagation terms  $h_1$  and  $h_{\Delta z}$  provide propagation priors, and trainable encoder-decoder modules refine this approximation. As illustrated in Fig. 2a, tiled input-image and phase-mask channels are first mapped through learned upsampling and coordinate or harmonic phase encodings, concatenated into a shared feature representation, and passed through a U-Net-style encoder, bottleneck and decoder with residual blocks, skip connections and channel embeddings. This refinement path learns residual aberrations, parasitic reflections and corresponding interferences, channel-dependent deviations and readout differences; the representative surrogate output shown in Fig. 2a has a generated-image MSE of about  $5 \times 10^{-4}$  relative to the ground-truth optical output. A single surrogate is shared across the implemented channel array. During training, newly measured optical pairs  $(\mathbf{x}, \boldsymbol{\theta}_{\text{phys}}, \mathbf{y}_{\text{phys}})$  are stored in a buffer and used to fine-tune  $\hat{f}$  online, allowing the differentiable model to track the physical system as the optical parameters evolve.

## Training ONN for vision tasks

We first train the multi-channel ONN in the independent-channel mode using MNIST classification (Fig. 2b–e). Different digit samples occupy different spatial channels, propagate through channel-specific trainable phase masks, and are read out from camera-plane detector tiles. The integrated

intensity in these detector regions forms a digit-score vector for each channel, so each channel produces its own class prediction while the optical hardware is used in parallel.

In this demonstration, the independent-channel model is implemented as a five-layer optical stack with 16 spatial channels and 1,003,520 trainable phase values, providing a direct test of whether many physical phase degrees of freedom can be coordinated across a shared multiplexed field. To increase the effective nonlinear interaction within this otherwise linearly propagating optical system, we also introduce a structural nonlinearity at the SLM plane. Here, structural nonlinearity denotes an input-dependent physical parameterization: the input pattern is embedded into the displayed SLM modulation, so that the optical operator depends jointly on the data and on the trainable phase profile rather than on the phase profile alone. This follows recent physical and optical neural-network schemes in which input-dependent scattering potentials, repeated data encodings, structural nonlinearities, or nonlinear optical encoders generate nonlinear functions using linear wave propagation<sup>20,22,24–26</sup>. Consistent with Eq. 1, for channel  $c$  at layer  $l$ , we write the displayed physical phase as  $\theta_{\text{phys},c}^{(l)} = \mathbf{T}_c^{(l)} \odot \mathbf{x}_c^{(l)} + \theta_{\text{train},c}^{(l)}$ , where  $\mathbf{x}_c^{(l)}$  is the encoded input to that channel and layer,  $\theta_{\text{train},c}^{(l)}$  is the trainable phase profile,  $\mathbf{T}_c^{(l)}$  controls the strength and spatial weighting of the input-dependent term, and  $\odot$  denotes pixelwise multiplication. This data-dependent modulation creates multiplicative interactions between the input, trainable phase, and diffractive propagation, expanding the optical feature space without requiring a separate nonlinear optical material. The channel-wise accuracy surface in Fig. 2c shows that the 16 channels improve over training with broadly similar trajectories, although some channel-dependent variation remains. The training and evaluation curves in Fig. 2d report the loss and accuracy obtained from the weighted sum of different channel readouts, showing that all channels are trained together within one multi-channel ONN rather than optimized as separate networks. The map in Fig. 2e summarizes this evolution across channels; the final average evaluation accuracy is approximately 86%, with individual channels ranging from 80.8% to 91.2%. These results show that spatially multiplexed channels can be trained as independent optical learners, while the remaining spread across channels indicates residual channel imbalance in the measured multi-channel system.

We next implement a class-code readout, in which the channel axis is used as a structured output space rather than as a set of independent classifiers (Fig. 3a). In this mode, the same input image is replicated across all optical channels, and each channel is read out through two spatial detector tiles corresponding to a binary response. The resulting channel-wise bit margins are decoded using a fixed codebook with 16 binary channels for 10 classes. The codebook is balanced: each class codeword contains eight +1 and eight -1 entries, and each channel assigns five classes to the positive bit and five classes to the negative bit. The minimum pairwise Hamming distance between class codewords is 8, with a mean distance of 8.89; specifically, 25 class pairs have distance 8 and 20 class pairs have distance 10, so every pair of classes differs in at least half of the 16 channels. This design turns the optical channel axis into a distributed class representation, where decisions are formed from the collective response of many channels rather than from a single readout. As a result, weak or noisy channels can be partially compensated by the remaining channel responses, and the large codeword separation provides robustness to channel imbalance and bit-level readout errors. Without inter-layer channel mixing or a trainable electronic feature mixer, the class-code optical model reaches approximately 92% test accuracy, showing that spatially multiplexed channels can serve as a robust structured readout dimension even when the optical channels remain independent until final codebook decoding.

Channel mixing provides a direct test of whether spatially multiplexed optical outputs can become an interacting feature representation rather than a collection of independent readouts. In the Fashion-MNIST demonstration, each input image is partitioned into a  $4 \times 4$  grid and mapped onto the 16 optical channels (Fig. 3b). Each channel therefore processes a local image patch through the optical stack, but after each optical layer the measured channel outputs are coupled by a simple electronic weighted sum before being re-encoded into the next optical layer. This hybrid coupling is not all-optical mixing; rather, it provides a controlled mechanism for exchanging information between optical channels while preserving the spatially multiplexed optical computation. The advantage is that local optical features are no longer forced to remain isolated: evidence distributed across patches can be integrated across layers, weak or noisy channel responses can be compensated

by the remaining channels, and the channel axis can act as an interacting feature dimension. In a five-layer optical architecture, this channel-mixed model reaches about 84% test accuracy, with a best evaluation loss of 0.5134 (Fig. 3c,d). These results show that even a simple electronic inter-channel weighted sum can turn spatial multiplexing from parallel optical processing into a trainable distributed representation for visual inference.

We then extend the multi-channel optical vision model from classification to continuous visual regression (Fig. 3e-h). The task is facial-keypoint detection: given a face image, the model predicts the two-dimensional locations of 15 facial landmarks, corresponding to 30 normalized output coordinates. The input face is partitioned across the 16 optical channels and processed through the multi-layer optical stack with channel mixing (Fig. 3e). The measured optical output is then pooled and mapped to the landmark coordinates by a lightweight electronic linear readout, keeping the task-specific digital head minimal. During training, the regression objective combines coordinate error with an output-mask penalty, and the reported pixel error is computed from the normalized-coordinate MSE as  $\sqrt{\text{MSE}} \times 96$  pixels. The five-layer optical model reaches a best evaluation MSE of  $6.57 \times 10^{-4}$ , corresponding to a pixel error of about 2.4 pixels (Fig. 3f,h). Representative held-out predictions localize landmarks around the eyes, nose, mouth and face contour (Fig. 3g). These results show that the hybrid multi-channel optical front end can support continuous spatial readout, extending the channel-based optical representation beyond class decisions to coordinate-level visual inference.

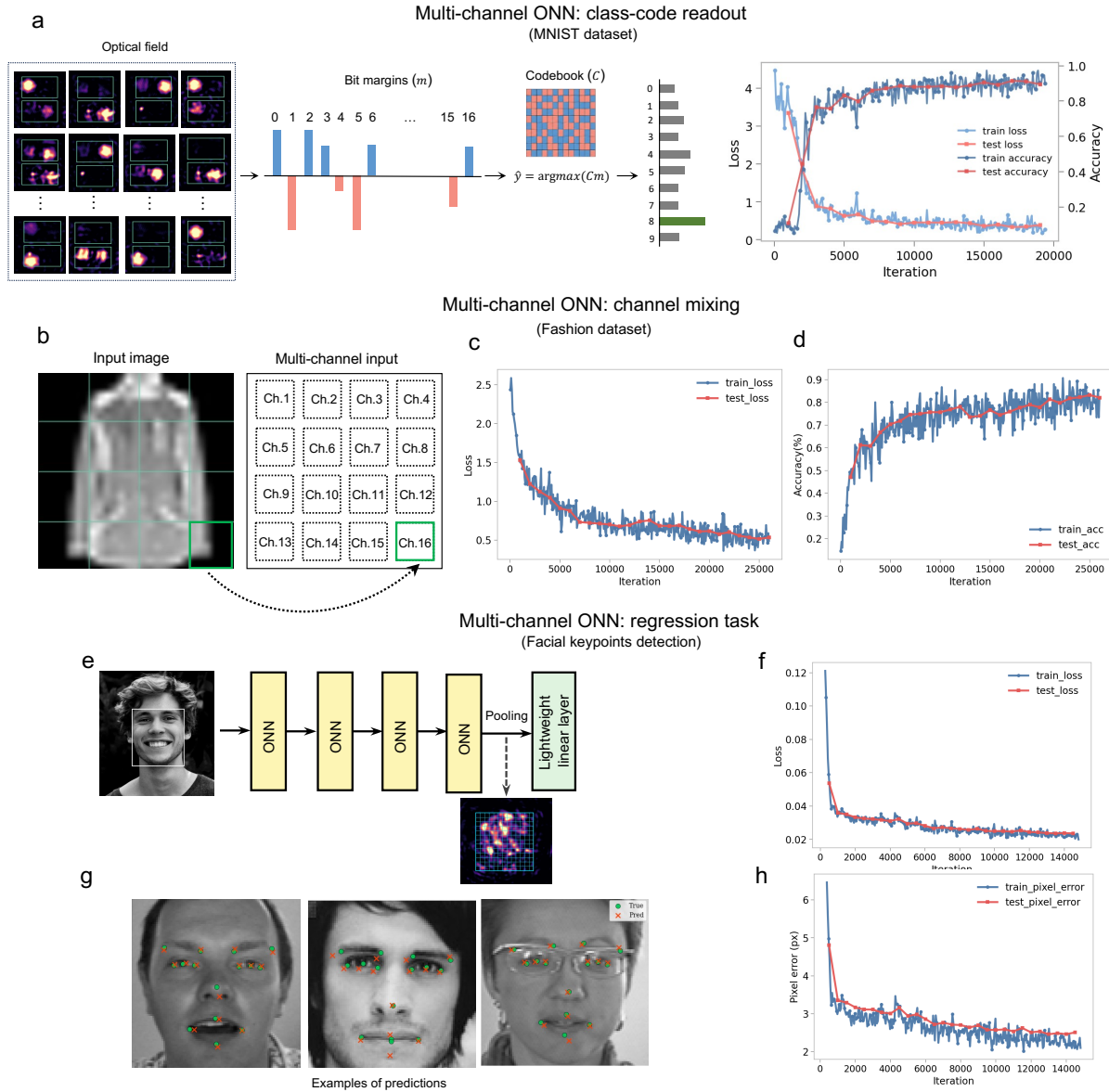


**Figure 3. Class-code readout, channel mixing, and facial-keypoint regression in multi-channel ONNs.** **a**, Class-code readout on MNIST. The tiled camera output is converted into channel-wise bit margins and decoded against a fixed  $10 \times 16$  class-code book; class scores are computed from code-matched projections, and the predicted class is selected by the largest score. **b**, Patchified channel input for channel mixing. A Fashion-MNIST image is partitioned into a  $4 \times 4$  grid, with one patch assigned to each optical channel. **c**, Training and evaluation loss for the five-layer Fashion-MNIST channel-mixing run. **d**, Training and evaluation accuracy for the same channel-mixing run, showing the fused classification performance. **e**, Facial-keypoint regression architecture. A face image is processed by the multi-channel optical stack, and the measured optical feature map is pooled and mapped by a lightweight electronic linear readout to 30 normalized landmark coordinates. **f**, Training and evaluation regression loss for facial-keypoint prediction. **g**, Representative held-out facial-keypoint predictions, with ground-truth landmarks in green and predicted landmarks in red. **h**, Pixel-error curves for facial-keypoint prediction, computed from normalized-coordinate MSE after conversion to the 96-pixel image scale.

## Optical vision-language model

Vision-language models commonly pair a visual encoder with a language decoder: the encoder converts an image into a sequence of visual tokens, and the decoder uses these tokens to generate text<sup>3,30–33</sup>. In a fully digital implementation, both the visual-token formation and the autoregressive text generation are performed electronically (Fig. 4a). Here we use the multi-channel optical neural network as the visual encoder/front end, while retaining a digital transformer decoder for sequence generation (Fig. 4b). In this hybrid architecture, optical propagation and trainable phase modulation produce image-conditioned visual tokens, which are then passed to the decoder in place of tokens produced by a digital transformer encoder. Thus, the optical system replaces the encoder-side visual computation of an encoder–decoder pipeline, while the language modelling, attention over text history and token generation remain digital. This provides a controlled starting point for optical vision-language processing: the optical network is not used merely as a classifier, but as a trainable visual-token generator for a downstream sequence model.

The training workflow follows the same physical-forward/surrogate-backward principle used in the classification and regression experiments (Fig. 4c). The input image is encoded into 16 optical channels, propagated through a six-layer optical stack and read out as a compact set of visual features for the transformer decoder. During the forward pass, these visual tokens are obtained from the measured optical response. During the backward pass, gradients with respect to the trainable optical phase parameters are supplied by the differentiable surrogate, with online fine-tuning from measured optical pairs. The decoder is trained to generate captions conditioned on the optical tokens and the previous text tokens. In this sense, the optical front end participates in the sequence-generation task through the visual representation it provides, while the text-generation mechanism itself remains electronic.

We evaluate this architecture on a controlled compositional captioning dataset designed to test whether the optical encoder can preserve object identity and spatial structure in a form usable by the decoder (Fig. 4d). Each image canvas is assembled from objects sampled from MNIST digits, Fashion-MNIST categories and NotMNIST letters, placed in fixed spatial slots such as the top-left,

top-right and bottom regions. The target caption describes both the identity and position of the objects, for example by specifying which digit, letter or fashion item appears in each slot. This task is intentionally more structured than open-vocabulary natural-image captioning, but it requires the optical encoder to provide visual tokens that retain multi-object and positional information across the channel array.

The hybrid optical-electronic model learns stable caption generation on this controlled task (Fig. 4e,f). The evaluation caption loss decreases throughout training and reaches a final value of 0.8712. Caption quality is evaluated using BLEU scores, a standard sequence-generation metric that compares generated captions with reference captions through modified  $n$ -gram precision and a brevity penalty. BLEU-1 measures word-level agreement, whereas BLEU-2, BLEU-3 and BLEU-4 progressively test longer phrase overlap and therefore provide stricter measures of sentence structure. In our controlled captioning task, high BLEU scores indicate that the decoder recovers both the object identities and the compositional caption template from the optical visual tokens. The final BLEU-1 through BLEU-4 scores are 0.9299, 0.9045, 0.8774 and 0.8479, respectively. More broadly, this result extends the role of the multi-channel optical neural network beyond fixed readout tasks: the same spatially multiplexed optical front end can supply task-relevant visual representations to a sequence model. Although the present demonstration uses a controlled captioning dataset and a digital decoder, it establishes a first step toward replacing digital visual encoders with trainable optical encoders in hybrid vision-language systems.

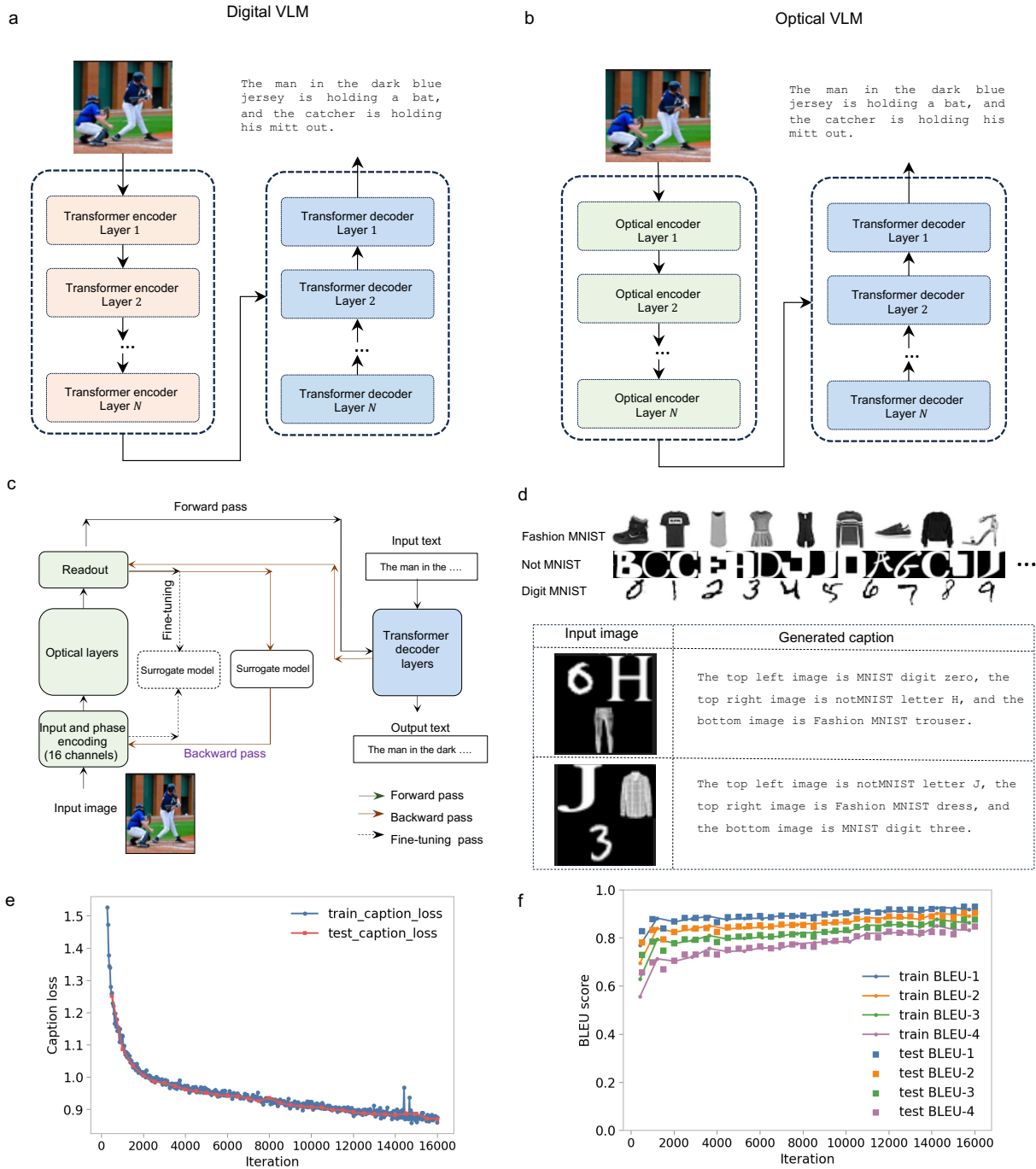


**Figure 4. Optical vision-language model with a digital transformer decoder.** **a**, Digital encoder-decoder captioning baseline, shown for architectural comparison. **b**, Hybrid optical-digital vision-language architecture, in which the optical stack replaces the visual encoder/front end while the transformer decoder remains digital. **c**, Training workflow for the optical vision-language model. The image is encoded into optical channels, propagated through optical layers, and read out as visual tokens for the decoder; the backward pass uses a differentiable surrogate, with optional surrogate fine-tuning from measured optical pairs. **d**, Controlled captioning dataset, composed from MNIST, Fashion-MNIST, and NotMNIST image slots with captions describing the top-left, top-right, and bottom objects. **e**, Caption cross-entropy loss curve for the optical vision-language run. **f**, BLEU-1 through BLEU-4 score curves for generated captions on the controlled captioning task.

## Discussion

This work shows that spatial multiplexing in optical neural networks can be used for more than parallel throughput. Across the demonstrations, the channel axis is progressively promoted from a hardware layout into a computational coordinate of the model. In the independent-channel experiment, multiplexing allows several optical learners to be trained within the same physical processor. In the class-code readout, the same channel array becomes a distributed output space, where a prediction is formed collectively from many binary optical responses rather than from a single detector region. This representation introduces redundancy: weak, noisy or imbalanced channels do not necessarily determine the final decision, because the codeword separation allows other channels to compensate. In the channel-mixing experiment, multiplexed optical outputs are no longer only read out in parallel, but are coupled between layers, allowing information distributed across spatial patches to interact during the computation. Together, these regimes demonstrate that the channel dimension can carry structured computational meaning.

The extension from classification to facial-keypoint regression and controlled caption generation further broadens this view. The regression task shows that the multi-channel optical front end can support continuous spatial outputs, not only discrete class decisions. The vision-language experiment then tests a more general role for the optical network: rather than acting as a classifier, it produces visual tokens for a downstream digital transformer decoder. This does not make the system a fully optical vision-language model, but it establishes an important architectural possibility. The optical processor can replace the visual-encoder side of an encoder–decoder pipeline, while the language decoder remains electronic. In this hybrid form, the optical system contributes trainable visual representations that are useful for sequence generation, pointing toward optical front ends that interface naturally with modern token-based machine-learning architectures.

A central enabling element is the online physical-forward/surrogate-backward training scheme. The forward pass is supplied by the measured optical system, so the optimization directly includes experimental effects such as aberrations, finite resolution, noise, drift and channel nonuniformity.

The surrogate is not used as a replacement for the optical processor; it is a differentiable interface that provides gradients for the trainable phase masks. Sharing a single channel-conditioned surrogate across the channel array is important because it preserves the common structure of the optical transformation while allowing channel-specific deviations to be corrected. Online fine-tuning further allows the surrogate to follow the physical system as the optical parameters evolve. This combination of measured forward computation and learned backward differentiation provides a practical route for training large, experimentally realized optical models with more than one million trainable phase parameters.

The present system is intentionally hybrid. Input preparation, camera readout, surrogate learning, inter-channel weighted mixing, lightweight regression heads and transformer decoding are performed electronically, while the optical stack provides the trainable physical transformation and measured visual representation. This division should not be viewed only as a limitation. It reflects a useful design principle for near-term optical machine learning: optical hardware can perform high-dimensional spatial transformations, while electronic computation supplies calibration, readout, sequence modelling and gradient-based optimization. More broadly, the results of this work suggest that spatial multiplexing should not be viewed solely as a strategy for increasing parallel throughput. Instead, the channel dimension can be incorporated directly into the model design and training process, serving as part of the learned representation itself.

Several directions follow naturally from this framework. More expressive and/or fully optical channel-mixing mechanisms could turn the channel axis into a deeper optical feature space. Future implementations could move some of these operations closer to the photonic domain, for example through integrated modulators, optical or optoelectronic channel mixing, faster detector feedback, or learned readout circuits. At the same time, the current free-space platform provides a flexible experimental test bed for exploring how optical degrees of freedom should be organized and trained. Extending the present hybrid vision-language demonstration toward a fully optical vision-language model represents another important direction. Such an architecture would require optical implementations of additional components that are currently electronic, including token generation,

sequence processing, attention-like operations, memory mechanisms, and language decoding. While these capabilities remain challenging, advances in integrated photonics, optical interconnects, nonlinear photonic devices, and optoelectronic feedback systems may enable progressively larger portions of the vision-language pipeline to be realized in the optical domain. In the longer term, such developments could move optical processors from trainable visual front ends toward more complete multimodal computing platforms.

## Methods

### Optical setup

The optical setup and its characterization is extensively presented in *Nætinger, Tuuva and Fleury*<sup>?</sup>. It has been explicitly conceived as a prototyping platform to investigate learning algorithms for diffractive neural networks (DNNs) using multiplexing to perform learning and inference in a reasonable amount of time, average noises or provide channel parallelism within the same setup.

A red laser beam at 633nm (Spectra Physics) is expanded using a  $4f$ -system (lens  $L_0$  and  $L'_0$ ). The resulting plane wave is directed to an amplitude modulator (Holoeye microdisplay HEO 2220 CFS with a  $4.5\mu\text{m}$  pixel pitch, referred to as *the microdisplay*) conjugated with a phase-only modulator (Holoeye ERIS with an  $8\mu\text{m}$  pixel pitch, referred to as *the SLM*) using a  $4f$ -system. The magnification of the  $4f$ -system is set so that one pixel of the microdisplay corresponds to one pixel of the SLM. The conjugation of the two modulators performs a multiplication of the field from the microdisplay convoluted by point-spread function  $h_1$  (taking into account the response of the  $4f$ -systems from the limited numerical aperture of lenses  $L_1$  and  $L_2$ ) and the phasemask on the SLM  $\exp(i2\pi\theta_{phys,c}^{(l)})$ . As the two modulators are conjugated,  $h_1$  corresponds to an Airy spot, its width is smaller than the size of a SLM pixels<sup>?</sup>. The resulting beam from the SLM is polarization filtered in a conjugate plane and then imaged onto a defocused camera. A diaphragm filters high spatial frequencies in the Fourier plane to reduce the experimental noises. The defocus allows to blend the input data. The amount of *mixing* is set by a tunable parameter  $\Delta z$  corresponding to the position of the camera relatively to the

conjugate plane, it sets the point-spread function  $h_{\Delta z}$ . The intensity readout of the camera makes the system non-linear. Thus, all the ingredients of convolutional neural networks are combined.  $N_c = 4 \times 4$  channels of  $N_{in,x} \cdot N_{in,y} = 128 \times 128$  pixels are defined both on the microdisplay and the SLM. As it is not possible to align each matching zone manually, each channel would have different transfer function mostly shifted, each zone are aligned thanks to a semi-automatic iterative procedure relying on sharp edge diffraction and automatic ellipse detection. It records the coordinates of the  $N_{in,x} \cdot N_{in,y}$  pixels associated to one channel for the microdisplay and SLM as well as the coordinates of the  $N_{out,x} \cdot N_{out,y}$  output pixels on the camera which are saved in a look-up table.  $N_b = 8$  acquisitions are performed successively. The interfacing code allows to create an object whose forward method takes the intensity and phasemask as *Pytorch* tensor inputs with shapes  $[N_c \cdot N_b, 1, N_{in,x}, N_{in,y}]$  and a  $[N_c \cdot N_b, 1, N_{out,x}, N_{out,y}]$  tensor as output from the camera readout. This function is fed to the neural network architecture and surrogate for learning.

## Data and code availability

The data and code used in this article are available at [MomeniAli/Multi-channel-OVM](https://github.com/MomeniAli/Multi-channel-OVM).

## References

1. Krizhevsky, A., Sutskever, I. & Hinton, G. E. Imagenet classification with deep convolutional neural networks. In *Advances in Neural Information Processing Systems*, vol. 25, 1097–1105 (2012).
2. He, K., Zhang, X., Ren, S. & Sun, J. Deep residual learning for image recognition. In *Proceedings of the IEEE Conference on Computer Vision and Pattern Recognition*, 770–778, [10.1109/CVPR.2016.90](https://doi.org/10.1109/CVPR.2016.90) (2016).
3. Dosovitskiy, A. *et al.* An image is worth 16x16 words: Transformers for image recognition at scale. In *International Conference on Learning Representations* (2021). [2010.11929](https://doi.org/2010.11929).
4. LeCun, Y., Bengio, Y. & Hinton, G. Deep learning. *Nat.* **521**, 436–444, [10.1038/nature14539](https://doi.org/10.1038/nature14539) (2015).
5. Sebastian, A., Le Gallo, M., Khaddam-Aljameh, R. & Eleftheriou, E. Memory devices and applications for in-memory computing. *Nat. Nanotechnol.* **15**, 529–544, [10.1038/s41565-020-0655-z](https://doi.org/10.1038/s41565-020-0655-z) (2020).
6. Wetzstein, G. *et al.* Inference in artificial intelligence with deep optics and photonics. *Nat.* **588**, 39–47, [10.1038/s41586-020-2973-6](https://doi.org/10.1038/s41586-020-2973-6) (2020).
7. Lin, X. *et al.* All-optical machine learning using diffractive deep neural networks. *Sci.* **361**, 1004–1008, [10.1126/science.aat8084](https://doi.org/10.1126/science.aat8084) (2018).
8. Liu, C. *et al.* A programmable diffractive deep neural network based on a digital-coding metasurface array. *Nat. Electron.* **5**, 113–122, [10.1038/s41928-022-00719-9](https://doi.org/10.1038/s41928-022-00719-9) (2022).
9. Mengu, D., Luo, Y., Rivenson, Y. & Ozcan, A. Analysis of diffractive optical neural networks and their integration with electronic neural networks. *IEEE J. Sel. Top. Quantum Electron.* **26**, 1–14, [10.1109/JSTQE.2019.2921376](https://doi.org/10.1109/JSTQE.2019.2921376) (2020).
10. Isil, C. *et al.* All-optical image denoising using a diffractive visual processor. *Light. Sci. & Appl.* **13**, 43, [10.1038/s41377-024-01385-6](https://doi.org/10.1038/s41377-024-01385-6) (2024).

11. Shen, Y. *et al.* Deep learning with coherent nanophotonic circuits. *Nat. Photonics* **11**, 441–446, [10.1038/nphoton.2017.93](https://doi.org/10.1038/nphoton.2017.93) (2017).
12. Feldmann, J. *et al.* Parallel convolutional processing using an integrated photonic tensor core. *Nat.* **589**, 52–58, [10.1038/s41586-020-03070-1](https://doi.org/10.1038/s41586-020-03070-1) (2021).
13. Xu, X. *et al.* 11 tops photonic convolutional accelerator for optical neural networks. *Nat.* **589**, 44–51, [10.1038/s41586-020-03063-0](https://doi.org/10.1038/s41586-020-03063-0) (2021).
14. Hua, S., Divita, E., Yu, S. *et al.* An integrated large-scale photonic accelerator with ultralow latency. *Nat.* **640**, 361–367, [10.1038/s41586-025-08786-6](https://doi.org/10.1038/s41586-025-08786-6) (2025).
15. Ahmed, S. R., Baghdadi, R., Bernadskiy, M. *et al.* Universal photonic artificial intelligence acceleration. *Nat.* **640**, 368–374, [10.1038/s41586-025-08854-x](https://doi.org/10.1038/s41586-025-08854-x) (2025).
16. Chen, Y., Nazhamaiti, M., Xu, H. *et al.* All-analog photoelectronic chip for high-speed vision tasks. *Nat.* **623**, 48–57, [10.1038/s41586-023-06558-8](https://doi.org/10.1038/s41586-023-06558-8) (2023).
17. Wang, T., Sohoni, M. M., Wright, L. G. *et al.* Image sensing with multilayer nonlinear optical neural networks. *Nat. Photonics* **17**, 408–415, [10.1038/s41566-023-01170-8](https://doi.org/10.1038/s41566-023-01170-8) (2023).
18. Wright, L. G., Onodera, T., Stein, M. M. *et al.* Deep physical neural networks trained with backpropagation. *Nat.* **601**, 549–555, [10.1038/s41586-021-04223-6](https://doi.org/10.1038/s41586-021-04223-6) (2022).
19. Xue, Z., Zhou, T., Xu, Z. *et al.* Fully forward mode training for optical neural networks. *Nat.* **632**, 280–286, [10.1038/s41586-024-07687-4](https://doi.org/10.1038/s41586-024-07687-4) (2024).
20. Momeni, A., Rahmani, B., Mallejac, M., del Hougne, P. & Fleury, R. Backpropagation-free training of deep physical neural networks. *Sci.* **382**, 1297–1303, [10.1126/science.adi8474](https://doi.org/10.1126/science.adi8474) (2023).
21. Momeni, A. *et al.* Training of physical neural networks. *Nat.* **645**, 53–61, [10.1038/s41586-025-09384-2](https://doi.org/10.1038/s41586-025-09384-2) (2025).

22. Hammami, C. *et al.* Expressivity of programmable-metasurface-based physical neural networks: encoding non-linearity, structural non-linearity, and depth, [10.48550/arXiv.2603.13602](https://arxiv.org/abs/10.48550/arXiv.2603.13602) (2026). [2603.13602](https://arxiv.org/abs/2603.13602).
23. Momeni, A. & Fleury, R. Electromagnetic wave-based extreme deep learning with nonlinear time-Floquet entanglement. *Nat. Commun.* **13**, 2651, [10.1038/s41467-022-30297-5](https://doi.org/10.1038/s41467-022-30297-5) (2022).
24. Xia, F. *et al.* Nonlinear optical encoding enabled by recurrent linear scattering. *Nat. Photonics* **18**, 1067–1075, [10.1038/s41566-024-01493-0](https://doi.org/10.1038/s41566-024-01493-0) (2024).
25. Yildirim, M. *et al.* Nonlinear processing with linear optics. *Nat. Photonics* **18**, 1076–1082, [10.1038/s41566-024-01494-z](https://doi.org/10.1038/s41566-024-01494-z) (2024).
26. Wanjura, C. C. & Marquardt, F. Fully nonlinear neuromorphic computing with linear wave scattering. *Nat. Phys.* **20**, 1434–1440, [10.1038/s41567-024-02534-9](https://doi.org/10.1038/s41567-024-02534-9) (2024).
27. Anderson, M. G., Ma, S.-Y., Wang, T., Wright, L. G. & McMahon, P. L. Optical transformers, [10.48550/arXiv.2302.10360](https://arxiv.org/abs/10.48550/arXiv.2302.10360) (2023). [2302.10360](https://arxiv.org/abs/2302.10360).
28. Xu, Z. *et al.* Large-scale photonic chiplet taichi empowers 160-tops/w artificial general intelligence. *Sci.* **384**, 202–209, [10.1126/science.adl1203](https://doi.org/10.1126/science.adl1203) (2024).
29. Chen, S., Li, Y., Wang, Y., Chen, H. & Ozcan, A. Optical generative models. *Nat.* **644**, 903–911, [10.1038/s41586-025-09446-5](https://doi.org/10.1038/s41586-025-09446-5) (2025).
30. Vaswani, A. *et al.* Attention is all you need. In *Advances in Neural Information Processing Systems*, vol. 30 (2017).
31. Vinyals, O., Toshev, A., Bengio, S. & Erhan, D. Show and tell: A neural image caption generator. In *Proceedings of the IEEE Conference on Computer Vision and Pattern Recognition*, 3156–3164, [10.1109/CVPR.2015.7298935](https://arxiv.org/abs/10.1109/CVPR.2015.7298935) (2015).
32. Xu, K. *et al.* Show, attend and tell: Neural image caption generation with visual attention. In *Proceedings of the 32nd International Conference on Machine Learning*, vol. 37 of *Proceedings of Machine Learning Research*, 2048–2057 (2015).

33. Radford, A. *et al.* Learning transferable visual models from natural language supervision. In *Proceedings of the 38th International Conference on Machine Learning*, vol. 139 of *Proceedings of Machine Learning Research*, 8748–8763 (2021).